



Effect of Microstructure and Phase Evolution on the Wear Behavior of Fe-Based Amorphous/Nanocrystalline Composite Coatings Synthesized by Plasma Spraying

Md Akif Faridi¹ · Sapan K. Nayak¹ · D. K. V. D. Prasad¹ · Amit Kumar¹ · Tapas Laha¹

Submitted: 3 November 2022 / in revised form: 19 June 2023 / Accepted: 29 June 2023 / Published online: 19 July 2023
© ASM International 2023

Abstract In this work, Fe-10Cr-10Mo-4B-2C-4P (wt.%) amorphous/nanocrystalline multilayered coatings were synthesized using the atmospheric plasma spraying method with different power/heat input to vary the degree of melting. Microstructural and compositional characterization results showed that both amorphicity and porosity decreased with increasing plasma power. Higher hardness was observed at elevated power due to the presence of less porosity and more amount of hard intermetallic phases in the amorphous matrix. Wear behavior of the coatings was investigated under two different modes viz. reciprocating mode and unidirectional rotating mode to reflect the real-life service conditions. Results of dry sliding wear test revealed that improved wear resistance for coatings synthesized at higher plasma power input is attributed to the formation of well-adhered splats and presence of higher amount of intermetallic phases. Interestingly, the specific wear rate and coefficient of friction values obtained by performing the wear test in rotating mode were lower compared to that in reciprocating mode. Most importantly, a transition in wear mechanism was envisaged as mode of wear changes, i.e., fatigue dominated in case of the reciprocating mode to abrasion dominated in the rotating mode.

Keywords atmospheric plasma spraying (APS) · crystallization · Fe-based amorphous/nanocrystalline composite coating · reciprocating wear · rotating wear · wear mechanism

Introduction

Metallic glasses (MGs) exhibit disordered atomic arrangement with unique combination of mechanical and corrosion properties (Ref 1-4). Fe-based MGs are more attractive among the different MG systems due to their excellent mechanical properties (Ref 5-7), good corrosion resistance (Ref 8-11) and soft magnetic properties (Ref 12-15). Alloying has a significant role in improving the glass forming ability (GFA) and mechanical properties of glassy alloys (Ref 16, 17). Wide variety of alloying elements, viz. Cr, Mo, Ni, Co, W, Zr, Y, Nb, W, etc., along with C, P and B are used in Fe-based amorphous alloys (Ref 18-22). However, by using industrially available low-cost alloying elements, Fe-based MGs can be made commercially more attractive. The aforementioned facts have resulted in significant attention toward the development of inexpensive Fe-based MG systems using relatively low-cost metalloids (C, P and B) and minimal addition of costly elements, like Cr and Mo in small quantity. In terms of wear behavior, Cr and Mo impart high hardness, while C, B and P improve the glass-forming ability of the alloy system along with the precipitation of hard intermetallics, which further increases the hardness and wear resistance (Ref 17, 23). Besides, monolithic amorphous alloys undergo catastrophic failure due to low plasticity, which restricts their widespread application. An effective way to avoid this limitation could be synthesizing Fe-based amorphous coatings, attributed to lower dimensional requirement

This article is part of a special topical focus in the *Journal of Thermal Spray Technology* on New and Emerging Markets in Thermal Spray. The issue was organized by Dr. Andrew Vackel, Sandia National Laboratories; Dr. John Koppes, TST Engineered Coating Solutions; Prof. Bertrand Jodoin, University of Ottawa; Dr. Dheepa Srinivasan, Pratt and Whitney; and Prof. Shrikant Joshi, University West.

✉ Tapas Laha
laha@metal.iitkgp.ac.in

¹ Department of Metallurgical and Materials Engineering, Indian Institute of Technology Kharagpur, Kharagpur, West Bengal 721302, India

(thickness) and the ease of synthesis (Ref 24). However, the inherent brittleness of Fe-based amorphous coating leads to reduction in wear resistance and impact toughness. The incorporation of nano-sized crystalline phases in an amorphous matrix improves mechanical properties by impeding shear band propagation (Ref 25). In recent years, Fe-based amorphous/nanocrystalline composite (Fe-ANC) coatings have received great attention from the scientific community for long-term surface protection (Ref 26, 27). When it comes to the development of metallic glass coatings, thermal spraying processes have been widely adopted, ascribed to their higher deposition rate and ease of operation (Ref 28–33). Among various thermal spraying processes, atmospheric plasma spraying (APS) is regarded as a simple and versatile technique to synthesize Fe-ANC coatings owing to very high cooling rate (10^7 – 10^8 K s⁻¹) associated with it, which promotes amorphous phase formation (Ref 32).

In engineering applications, especially where the structural components are in contact with each other, surfaces are prone to be damaged by wearing process. In this regard, it is of significant importance to understand the wear behavior of amorphous coatings. Numerous work has been carried out to investigate wear behavior of Fe-based amorphous coatings synthesized by different methods, such as HVOF (Ref 31, 34), HVAF (Ref 35), APS (Ref 32), cold spray (Ref 36), D-gun spray (Ref 37), etc. Luo et al. prepared plasma sprayed Fe-ANC coatings with different heat inputs and found that higher plasma power resulted in the formation of dense coating with nanocrystalline phase formation, leading to improvement in mechanical properties (Ref 38). It has been reported that the wear process under dry sliding condition is dominated by abrasion and delamination mechanisms. Kumar et al. reported that Fe-ANC coatings produced at higher plasma power exhibited excellent wear resistance under reciprocating mode wear test due to better inter-splat bonding and higher amount of nanocrystalline intermetallic phases in the coatings (Ref 39). Ma et al. fabricated Fe-based amorphous coating by HVOF process and analyzed its wear behavior under reciprocating mode and deduced that oxidation wear as the dominant phenomenon during the wearing process (Ref 40). Li et al. studied the wear behavior of Fe-ANC coatings deposited by D-gun spray method under rotating mode of dry sliding wear condition (Ref 41). They reported that the wear rate of Fe-based amorphous coatings was more sensitive to applied sliding speed rather than the applied normal load, and wear mechanism changed from delamination to oxidative as sliding speed increased.

From the above-mentioned literature review, it is evident that the research on wear behavior of Fe-based amorphous coatings is mostly concentrated either on correlating the microstructure and phase evolution with the

wear property or finding relationship of testing parameters, such as speed, load, etc., on wear resistance. Moreover, these studies are based either on reciprocating or on rotating mode of sliding wear. Therefore, a comprehensive understanding of difference in wear behavior along with the corresponding degradation mechanism during reciprocating and rotating modes of dry sliding wear behavior is crucial.

Accordingly, in this work, Fe-ANC coatings (Fe-10Cr-10Mo-4B-2C-4P, wt.%) were deposited on mild steel substrate by APS process with varying heat input to vary the degree of melting. The effect of plasma spraying power on microstructural development, phase evolution and their combined effect on the mechanical and tribological properties of the coatings are elucidated. The primary focus of this work includes in-depth understanding of wear process and corresponding mechanism of Fe-ANC coatings during different modes of sliding wear, i.e., rotating and reciprocating. This work highlights the difference in wear process of Fe-ANC coatings between reciprocating and rotating mode of dry sliding wear performed under similar experimental conditions.

Experimental Procedure

Synthesis of Fe-Based Amorphous/Nanocrystalline Coatings

Fe-based feedstock powder of composition Fe-10Cr-10Mo-4B-2C-4P (wt.%), synthesized by water atomization with a size range of 10–60 μm, procured from Innomet Powders, India, was used for coating deposition. The coatings were deposited onto mild steel substrate (dimension of 50 mm × 30 mm × 3 mm) by atmospheric plasma spraying process using a MP 200 APS system (AMT^{AG} Adv. Mat. Tech., Switzerland). Table 1 presents the parameters used for the plasma spraying. Coatings prepared under 20, 30 and 40 kW have been denoted as Coat-L, Coat-M and Coat-H, respectively.

Fully amorphous ribbons of the same composition were synthesized via melt spinning for quantitatively comparing the amorphous phase present in the feedstock powder and coatings. To prepare amorphous alloy ribbons, alloy ingots were produced by vacuum arc melting of feedstock powder under argon atmosphere. Ingots were remelted at least five times to achieve better chemical homogeneity. Melt-spun ribbons were produced by rapidly injecting the alloy melt onto Cu-Be wheel rotating with a peripheral velocity of 40 m/s.

Table 1. Process parameters used for synthesizing Fe-based amorphous/nanocrystalline composite coatings by atmospheric plasma spraying process

Coatings	Plasma power (kW)	Primary gas (Ar) flow rate, L/min	Secondary gas (H ₂) flow rate, L/min	Spray distance, mm	Powder feed rate, g/min	Coating thickness, μm
Coat-L	20	60	10	110	40	400-450
Coat-M	30					
Coat-H	40					

Characterization of Coatings

Microstructural examination of feedstock powder and all the three coatings was carried out by scanning electron microscope (SEM) using an FESEM, Merlin Gemini II (Zeiss, Germany). Porosity content of the coatings was estimated from polished cross-sectional surface using area analysis technique with ImageJ software version k1.45 from at least fifteen micrographs in each case. Phase analysis in feedstock powder and all the three coatings was carried out by x-ray diffraction (XRD) using a D8 Advance diffractometer (Bruker, Germany) using Cu K α radiation ($\lambda = 1.54 \text{ \AA}$). From the XRD spectra, area of crystalline peaks and amorphous humps was measured, and Eq 1 is used to calculate the amorphous phase fractions (Ref 42, 43).

$$V_{\text{amor}} = \frac{A_{\text{amor}}}{A_{\text{amor}} + A_{\text{cryst}}} \quad (\text{Eq 1})$$

where A_{cryst} , A_{amor} and V_{amor} are the areas of crystalline peaks, area of amorphous humps and the fraction of the amorphous phase content (by volume), respectively. Phase evolution was further investigated by transmission electron microscopy (TEM) using a Tecnai G² 30ST (FEI Company, USA). Thermal stability of the feedstock powder and coatings was analyzed by differential scanning calorimetry (DSC) using a DSC 8000 (PerkinElmer, USA) with a heating rate of 10 K/min in the temperature range of 30–750 °C under nitrogen atmosphere. Volume fraction of amorphous and crystalline phases in the coatings was also estimated from the obtained DSC thermograms. Approximate amount of crystalline phases present in the coatings prepared at different spraying power is calculated by Eq 2 (Ref 43, 44)

$$V_{\text{cryst}} = 1 - \frac{\Delta H_{\text{coating}}}{\Delta H_{\text{ribbon}}} \quad (\text{Eq 2})$$

where V_{cryst} represents volume fraction of crystalline phase in the coating, $\Delta H_{\text{coating}}$ and ΔH_{ribbon} are the total enthalpies released on crystallization of coating and fully amorphous ribbon, respectively. Moreover, the fraction of the amorphous phase in the coatings is estimated by Eq 3.

$$V_{\text{amor}} = 1 - V_{\text{cryst}} = \frac{\Delta H_{\text{coating}}}{\Delta H_{\text{ribbon}}} \quad (\text{Eq 3})$$

where V_{amor} represents volume fraction of amorphous phase in the coating.

Hardness was measured at both micro- and nano-level. Microhardness of the coatings was carried out by Vickers microindenter using a UHLMHT–001 (Walter Uhl, Germany). A vertical load of 25 gf was applied for 15 s to evaluate the hardness of the coatings. Nanoindentation study was performed using a TI 950 TriboIndenter (Hysitron Inc., USA) with a Berkovich tip under a peak load of 5000 μN, a loading and unloading rate of 500 μN s^{−1} and a holding time of 10 s. A minimum of 100 indentations were performed to estimate the average nanohardness of the coatings. Dry sliding wear experiment was performed by a TRB³ ball-on-disc tribometer (Anton Paar Netherlands) with 6 mm diameter of alumina ball as the counter body in reciprocating and unidirectional rotating mode at room temperature. For reciprocating mode, a sliding stroke of 6.3 mm and a frequency of 3 Hz were used. To ensure the same average sliding speed, rotating mode was carried out at 38 mm/s with wear track diameter of 2 mm. The normal load was 10 N, and total sliding distance was 150 m for both the wear modes. The wear resistance of the coatings has been represented by wear rate, which was calculated by the equation $Q = \frac{V}{N \cdot S}$, where Q is the specific wear rate (mm³ N^{−1} m^{−1}), V is the wear volume (mm³), N is the applied load (N) and S is the sliding distance (m), respectively. The wear volume (wt. of wear loss / density of coating) was measured from the weight loss of the samples after performing the wear test. Worn surfaces of the specimens were examined under SEM for examining the wear track morphology and investigating the effect of microstructure on wear behavior and the corresponding wear mechanisms. Before SEM analysis, indentation study and wear testing, the coatings were sequentially polished by emery paper from 400 to 2000 grit size, followed by polishing with diamond paste of 6, 1 and 0.25 μm paste. Finally, the samples were ultrasonicated in ethanol followed by drying in air to clean the surface.

Results and Discussion

Feedstock Powder: Morphology and Phase Evolution

SEM image of the feedstock powder synthesized by water atomization process is represented in Fig. 1a. Characteristic of the powder particles was found mostly as spherical with varying size range of 10–60 μm. Particle size distribution of the feedstock powder is represented as a histogram along with cumulative frequency curve as shown in Fig. 1b, and it was found that the majority of the particle size falls in the range of 20–40 μm. Phase analysis of the feedstock powders was performed by XRD, and the pattern is shown in Fig. 1c, which displays broad hump between 35° and 55° angle and several overlapped diffraction peaks. Combination of a broad halo hump with some crystalline peaks in the XRD pattern confirms the amorphous/crystalline nature of the feedstock powder. The identified crystalline peaks matched well with Fe₂B (PDF No. #00-036-1332), Fe₃B

(PDF No. #00-039-1315), FeP₂ (PDF No. #00-006-0561), Fe₅PB₂ (PDF No. #00-017-0390), Mo₂C (PDF No. #00-045-1014), FeB (PDF No. #00-032-0463), Fe₃Mo₃C (PDF No. #00-047-1191), Fe₃Mo (PDF No. #00-031-0641), Cr₇BC₄ (PDF No. #00-019-0324) and Cr₂₃C₆ (PDF No. #00-035-0783) phases.

Microstructure of the Coatings

Figure 2 illustrates the SEM images of the as-sprayed and polished top surfaces of coatings sprayed at different plasma powers. As depicted in Fig. 2a, the coating sprayed with the lowest plasma power of 20 kW exhibits many unmelted particles along with significant porosity on the surface. It can be deduced that lower plasma power was insufficient to melt the high proportion of powder particles, resulting in a less compact coating. As the heat input increased by increasing the plasma power to 30 and 40 kW, the proportion of unmelted and partially melted particles is decreased, which resulted in a reduction of both size and

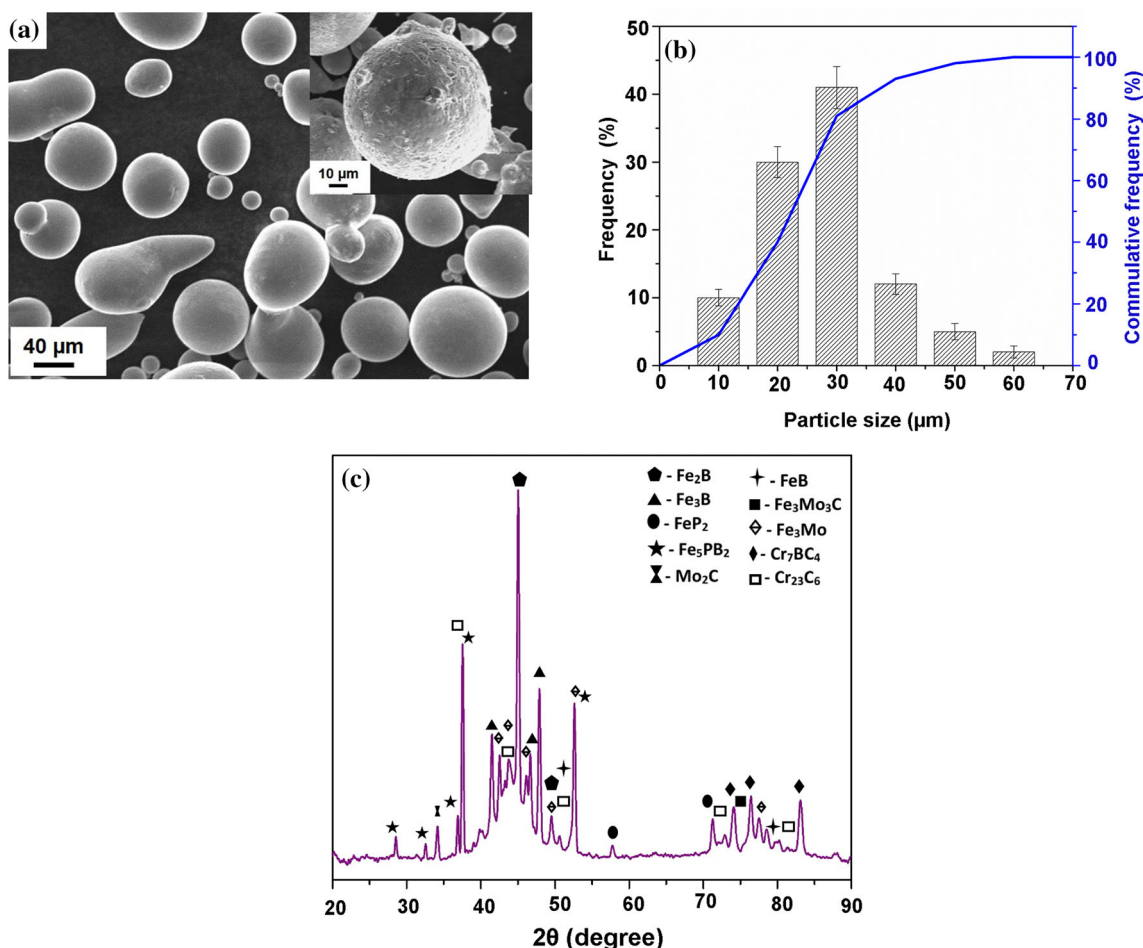
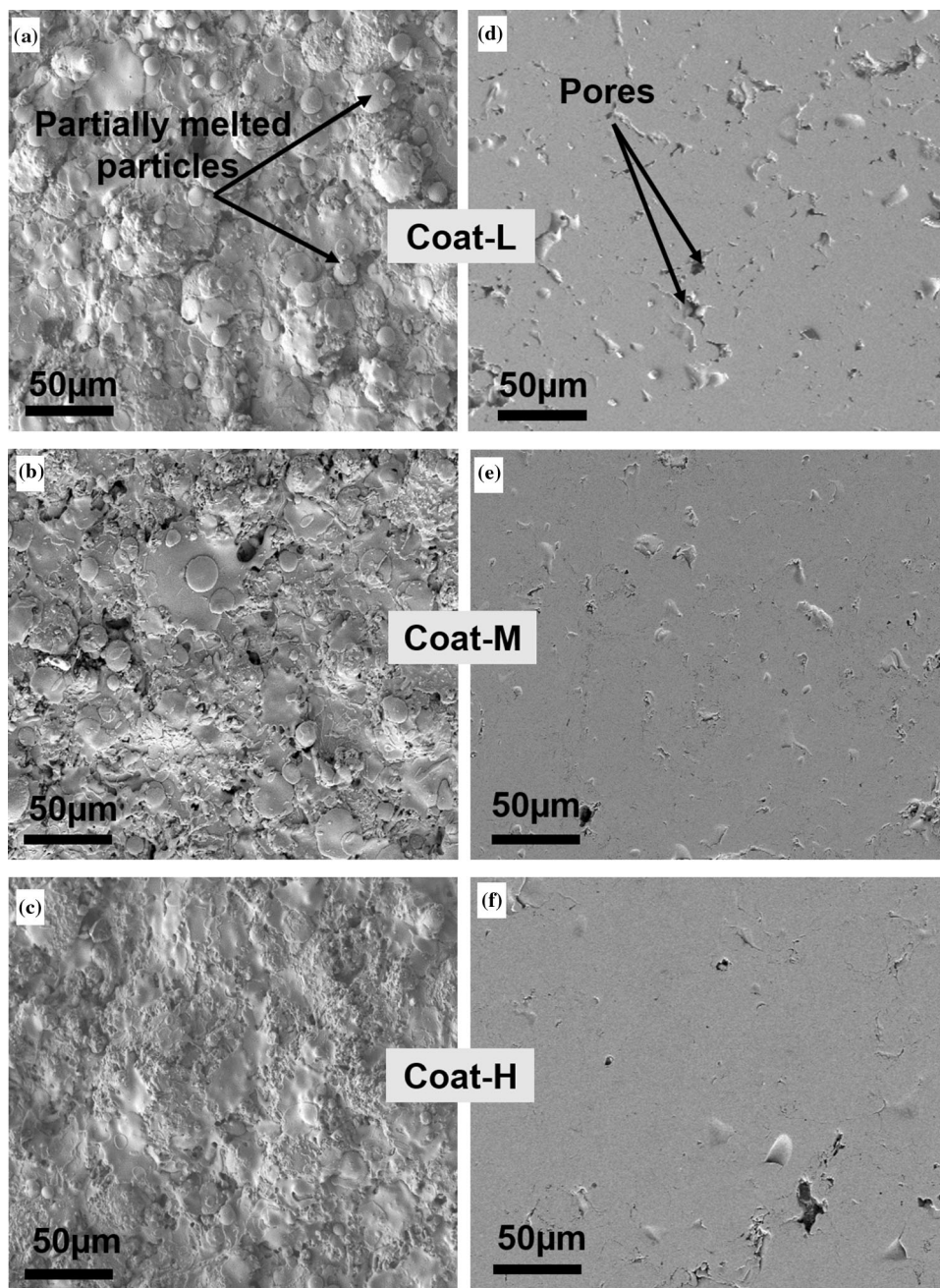


Fig. 1. (a) SEM micrograph, (b) particle size distribution and (c) XRD pattern of the Fe-based (Fe-10Cr-10Mo-4B-2C-4P, wt.%) water atomized feedstock powder

Fig. 2. SEM micrographs of (a–c) as-sprayed and (d–f) polished top surfaces of the plasma sprayed coatings



amount of the porosity in the coating (Fig. 2b and c). In general, the presence of both unmelted and partially melted particles in the coating increases the porosity content. As a result, bonding between the splats in the coating becomes weaker. Quantity of the porosity present in different coatings is measured as 5.3, 2.9 and 2.1% for coatings sprayed at 20 kW, 30 kW and 40 kW, respectively, as reported in Table 2. At higher plasma power, high temperatures are attained leading to adequate heating of the powder particles, which results in good melting (Ref 37, 38).

Phase Analysis of the Coatings

XRD patterns of the coatings and melt-spun ribbon are shown in Fig. 3. XRD pattern of the ribbon exhibits wide hump between 35° and 55° angle without any diffraction peak, while the coatings display broad humps and several overlapped diffraction peaks. The presence of wide hump was due to amorphous phase, while the diffraction peaks were formed because of the crystalline phases as mentioned earlier in the discussion of the XRD pattern obtained from the feedstock powder. Thus, the ribbon was of fully amorphous nature subjected to very high cooling rate

Table 2 Quantification of various microstructural feature and mechanical properties of the plasma sprayed coatings

Properties	Plasma power (kW)		
	20	30	40
Porosity content (vol.%)	5.34 ± 1.64	2.94 ± 0.81	2.18 ± 0.40
Amorphous phase content (vol.%)	86.6	81.3	78.8
Vickers hardness ($H_{V0.025}$)	1006 ± 30	1157 ± 52	1283 ± 48
Nanohardness (GPa)	12.06 ± 1.46	12.5 ± 1.32	14.06 ± 1.08
Specific wear rate, reciprocating (10^{-5} mm ³ /N m)	3.97 ± 0.20	3.10 ± 0.14	1.59 ± 0.13
Specific wear rate, rotating (10^{-5} mm ³ /N m)	3.32 ± 0.18	2.22 ± 0.14	0.76 ± 0.13
COF (reciprocating)	0.77 ± 0.20	0.59 ± 0.14	0.41 ± 0.13
COF (rotating)	0.57 ± 0.17	0.48 ± 0.11	0.17 ± 0.09

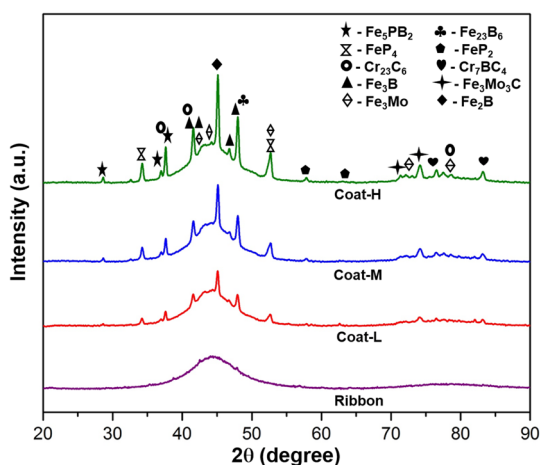


Fig. 3. XRD patterns of the different coatings deposited with varying plasma power and the completely amorphous ribbon of similar composition showing variation in crystallization

during melt spinning, while the three coatings showed amorphous/crystalline composite nature. The relative amount of amorphous phase present in the coatings obtained at different spraying power is calculated by Eq 1 and found as 86.6, 81.3 and 78.8% for Coat-L, Coat-M and Coat-H, respectively. Decreasing trend of amorphization with increasing spraying power was due to the higher degree of melting of feedstock powder at higher spraying power and more probability for the formation of crystalline phase during solidification. The identified crystalline peaks matched well with Fe₃Mo (PDF No. #00-031-0641), Fe₃Mo₃C (PDF No. #00-047-1191), Mo₂C (PDF No. #00-045-1014), Fe₂B (PDF No. #00-036-1332), Fe₃B (PDF No. #00-039-1315), Fe₂₃B₆ (PDF No. #00-047-1332), Fe₅PB₂ (PDF No. #00-017-0390), FeP₂ (PDF No. #00-006-0561), FeP₄ (PDF No. #00-040-1003), Cr₂₃C₆ (PDF No. #00-035-0783) and Cr₇BC₄ (PDF No. #00-019-0324) phases.

To investigate thermal stability of the phases present in the coatings, DSC was carried out, and the thermograms are shown in Fig. 4. The presence of exothermic peak observed for the powder, coatings and ribbon confirms the

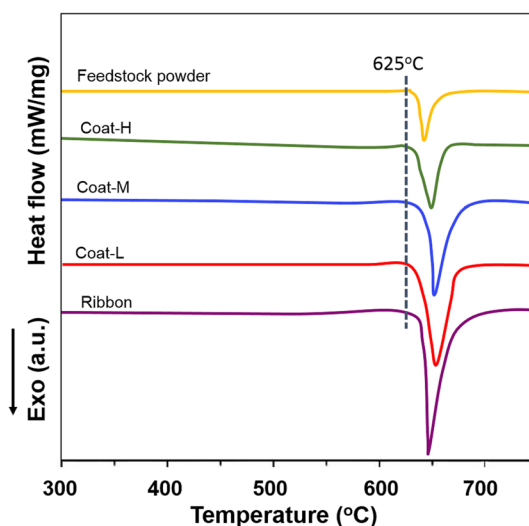


Fig. 4. DSC thermograms of the different coatings, completely amorphous melt-spun ribbon and feedstock powder

phase transformation from amorphous phase to crystalline phases. Enthalpy of crystallization is estimated to be – 90, – 69, – 63, – 60 and – 37 J/g for completely amorphous ribbon, Coat-L, Coat-M, Coat-H and feedstock powder, respectively. Higher negative enthalpy of crystallization is an indicator of higher degree of amorphicity. The relative amount of amorphous phase presents in the coatings prepared at different spraying power is calculated by Eq 2 and found as 76.7, 70.0, and 66.7 and 41.1% for Coat-L, Coat-M, and Coat-H and feedstock powder, respectively, considering ribbon to be 100% amorphous. Therefore, the amorphous content estimated by DSC analysis decreased in the order of ribbon, Coat-L, Coat-M, Coat-H and feedstock powder, which is consistent with the XRD analysis presented above. Inconsistency observed in volume fraction of amorphous phase obtained from XRD and DSC data could be due to the variation in interfacial energy of the glassy matrix and nanocrystalline phase interface, and probable inaccuracy in baseline correction (Ref 42, 43).

Fig. 5. (a) TEM micrograph of the coating and (b) corresponding SAD pattern showing the presence of nano-sized grains embedded in the amorphous matrix

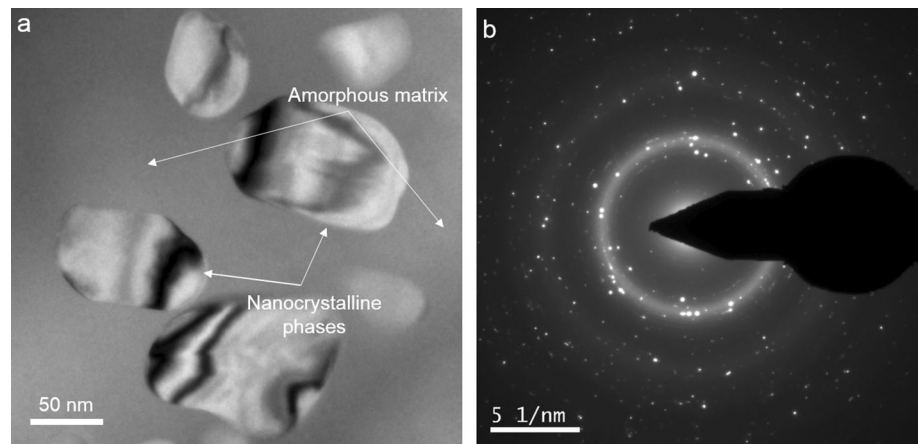
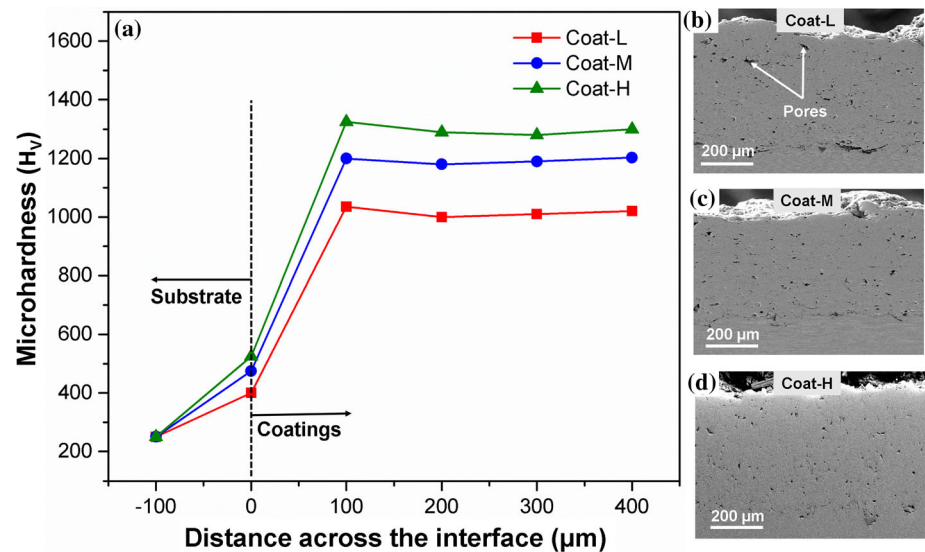


Fig. 6. (a) Vickers microhardness profile and (b, c, d) cross-sectional SEM images of the coatings



TEM was carried out to study the phase evolution in the coatings and to substantiate the composite structure. A representative TEM micrograph and corresponding selected area diffraction (SAD) pattern of Coat-M are shown in Fig. 5. Distribution of nanocrystalline phases can be clearly observed from Fig. 5. It was envisaged that nanocrystalline phases are uniformly distributed in the amorphous matrix, and this observation is complimented with the corresponding SAD pattern, which showed spots overlapped on broad diffused background.

Micro- and Nano-hardness of the Coatings

Hardness of the coatings was characterized at both micro- and nano-scale. Figure 6a shows the microhardness profile along the cross section of the coatings, and Fig. 6(b), (c) and (d) represent the corresponding cross-sectional SEM images. Microhardness values of the coatings were measured as 1006 ± 30 , 1157 ± 52 and 1283 ± 48 H_V for Coat-L, Coat-M and Coat-H, respectively. From the

aforementioned microhardness results, it is noted that the microhardness value steadily increased as the spraying power was increased. This was due to higher extent of melting at higher spraying power, which would have filled up the pores generated in the previously deposited splats, resulting in the formation of a more compact coating. Consequently, size and quantity of the pores reduced (Fig. 6b, c, d), which contributed to the enhanced hardness. Additionally, coating synthesized at higher spraying power contained more amount of hard intermetallic phases, which contributed to increasing the hardness of the coatings (Ref 39, 44)

To further evaluate the hardness and the distribution of various phases in the coatings, grid indentation technique (10×10 matrix of indentation) was employed. Average nanohardness of Coat-L, Coat-M and Coat-H was found to be 12.06 ± 1.46 , 12.5 ± 1.32 and 14.06 ± 1.08 GPa, respectively, as reported in Table 2. Nanohardness of the coatings has been plotted against the percentage number of indents for quantitative approximation of hardness of the

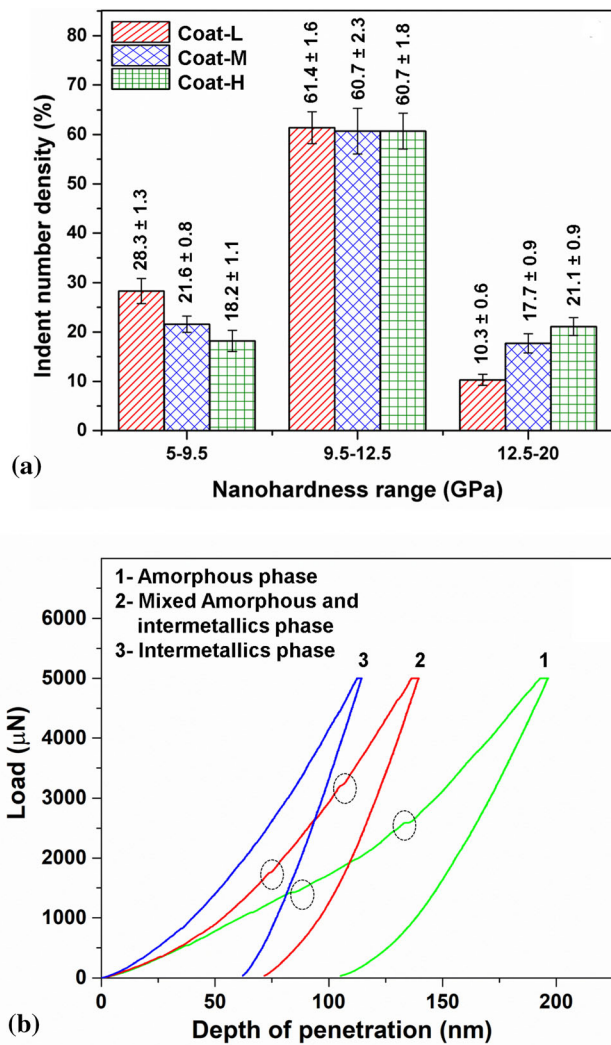


Fig. 7. (a) Bar graph showing the indent number density (%) of the plasma sprayed coatings in three different nanohardness range, viz. 5-9.5 GPa, 9.5-12.5 GPa and 12.5-20.0 GPa, representing amorphous matrix, mixed amorphous matrix and intermetallic phase and intermetallic-rich regions, respectively, and (b) typical load versus penetration depth plots obtained from nanoindentation test for different phases in the coatings (enclosed circles in Fig. 7b represent pop-ins)

different phases. The obtained nanohardness range is divided into three sets, based on the previous reports, viz. 5.0-9.5 GPa, 9.5-12.5 GPa and 12.5-20.0 GPa, belonging to (i) amorphous matrix, (ii) mixed amorphous and nano-sized Fe-based intermetallic phases and (iii) nano-sized intermetallic-rich regions, respectively (Ref 17, 28, 38, 41). It is to be noted that hardness of the different phases was not changing, and only the fraction of various phases with different hardness was varying, which ultimately resulted in different levels of overall hardness for the coatings sprayed with varying plasma powers. Indent number density versus nanohardness plot is useful for quantitative approximation of different phases present in multiphase

materials. Figure 7a represents the indent number density (%) with hardness range, and Fig. 7b shows typical load versus penetration depth plots obtained from nanoindentation test for different phases in the coatings. From Fig. 7a, it can be inferred that the indent number density (%) corresponding to the hardness range of 5-9.5 GPa, which represents the hardness of amorphous phase is decreasing with the increase in heat input. However, the percentage of indents falling on the intermetallic phase-rich regions with the hardness range of 12.5-20.0 GPa increased at higher heat input. This is because of the coating synthesized at higher heat input contained less amount of amorphous phase and higher amount of intermetallic crystalline phases, as discussed in section “Phase Analysis of the Coatings.” One interesting point to note here is that the maximum percentage of the indenter fell on the mixed amorphous and intermetallic phases corresponding to nanohardness range 12.5-20.0 GPa in all coatings. This confirms that most of the nanocrystalline phases were uniformly distributed in the matrix. Additionally, pop-in events in the load–displacement curves (Fig. 7b) of amorphous and mixture of amorphous and intermetallics phases indicated the glassy nature of the coatings, as these pop-ins generated during nanoindentation represent the initiation and/or propagation of shear bands in the glassy phase (Ref 3, 4).

Wear Behavior of the Coatings

Figure 8 shows the coefficient of friction (CoF) versus Sliding distance plots of the coatings obtained from reciprocating and rotating modes of dry sliding wear tests. It can be observed that CoF increased at the very beginning of the sliding process and then decreased to some extent followed by a continuous increase in CoF values till constant value. The initial increase in CoF is attributed to the small contact area (Ref 33). As the sliding process continued, delamination of the coatings occurred and the surface became rough and internal porosities were exposed, which led to increase in the CoF. Due to continuous and repetitive sliding, localized heating and oxidation occur and stress is generated in the coatings, which leads to initiation of cracks. On further sliding, these cracks propagate and delamination occurs for a layer on the top of the coating because of lower degree of cohesion between the frictional heating-induced oxidized part of the coating and unoxidized region below oxidized areas, leading to spallation of the oxidized layer. In the final stage, the process of generation and spallation of wear debris on the surface reached a steady state, and oxide film formation might have occurred on the worn surface as well, causing CoF to get stabilized and not increase further. Fluctuations in CoF curve during sliding are observed to be higher for Coat-L

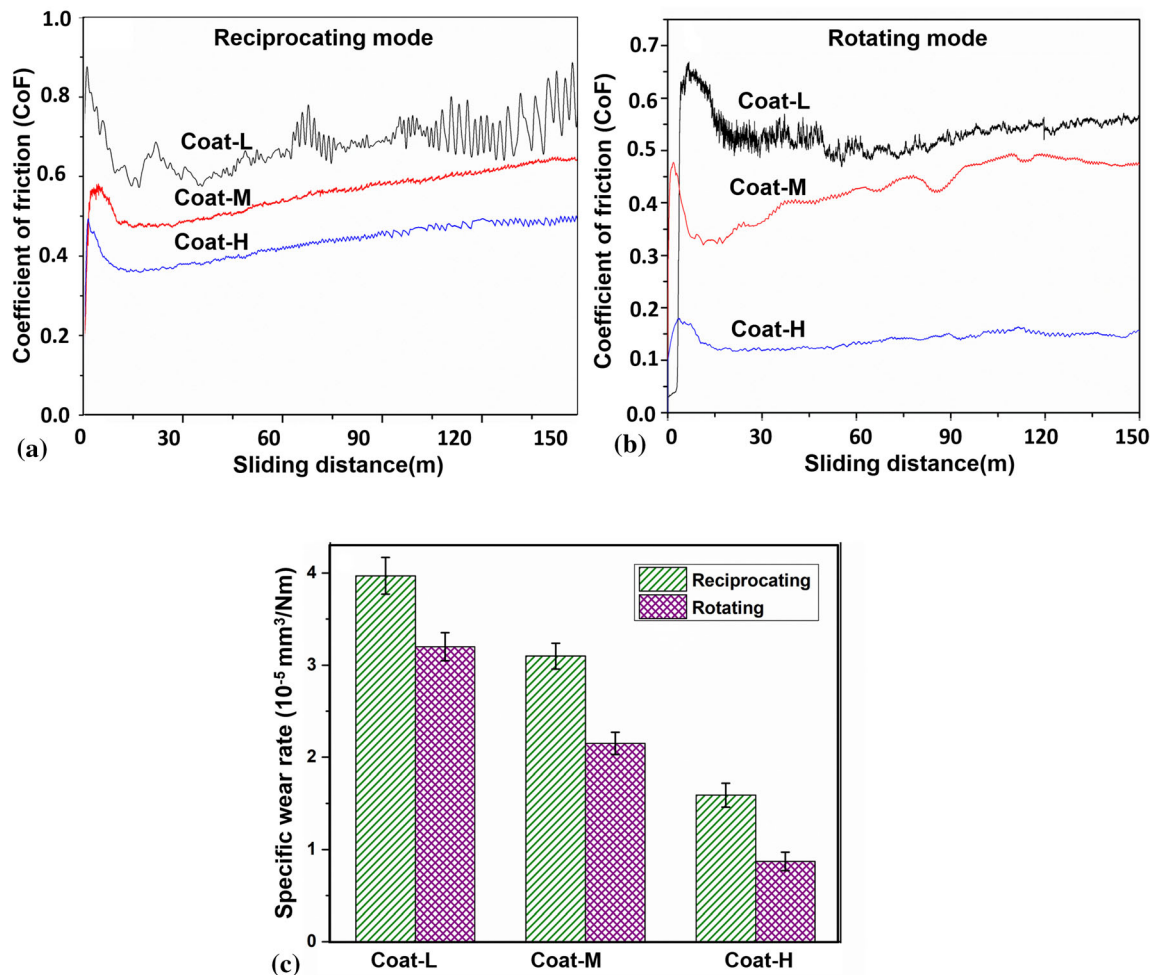


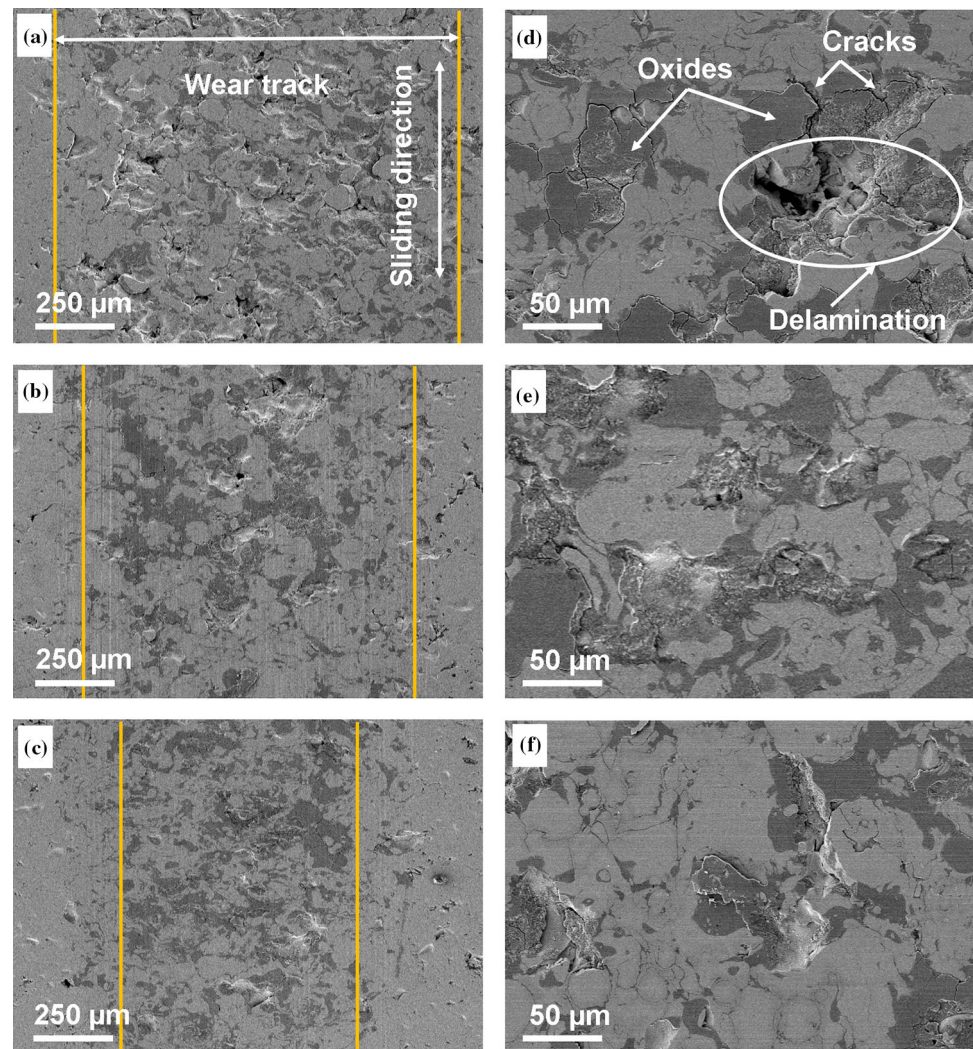
Fig. 8. (a, b) Variation in coefficient of friction with sliding distance obtained from dry sliding wear test carried out in reciprocating and rotating mode, respectively, and (c) specific wear rate of the coatings in different modes

compared to Coat-M and Coat-H due to relatively poor inter-splat bonding along with bigger pores observed in Coat-L. Lowest CoF for Coat-H was due to the highest hardness and least porosity content among the three coatings (Ref 45). The average CoF values of the coatings in reciprocating mode were 0.77 ± 0.20 , 0.59 ± 0.14 and 0.41 ± 0.13 , while for rotating mode were 0.57 ± 0.17 , 0.48 ± 0.11 and 0.17 ± 0.09 , corresponding to the spraying power 20 kW, 30 kW and 40 kW, respectively. An interesting point to note here is that, despite keeping the total sliding distance, track length and average sliding speed same in both reciprocating and rotating modes of sliding as mentioned in the experimental procedure, CoF values obtained in reciprocating mode were higher than those of the rotating mode. Average sliding speed in both modes, i.e., reciprocating and rotating modes were kept identical but in reciprocating mode of wear test, sliding speed is varied from zero at the extreme edges to 78 mm/s at the center of the wear track. Since maximum sliding speed is significantly higher than the average sliding speed

in reciprocating mode, thereby causing the counter body to impact more energy around the already delaminated and/or defective regions, leading to spallation in the coating. In rotating mode, sliding speed is constant throughout the wear track, and counter body impacts less energy compared to reciprocating mode causing less damage. Additionally, in reciprocating mode of wear, higher amount of debris particles remains on the wear track, while in the rotating mode, centrifugal force throws the debris particles away from the wear track, and these debris particles can act as an interfacial medium, leading to larger friction in the reciprocating mode.

Figure 8c graphically shows the variation in specific wear rate of the coatings after reciprocating and rotating mode of dry sliding wear tests. It can be observed that the specific wear rate of the coatings is decreased at higher spraying power in both reciprocating and rotating mode of wear tests. This is ascribed to the higher hardness and higher compactness (lower porosity) of the coating synthesized at higher spraying power. Moreover, the wear rate

Fig. 9. Worn surface morphology of the coatings after reciprocating mode dry sliding wear test: (a, d) Coat-L, (b, e) Coat-M and (c, f) Coat-H

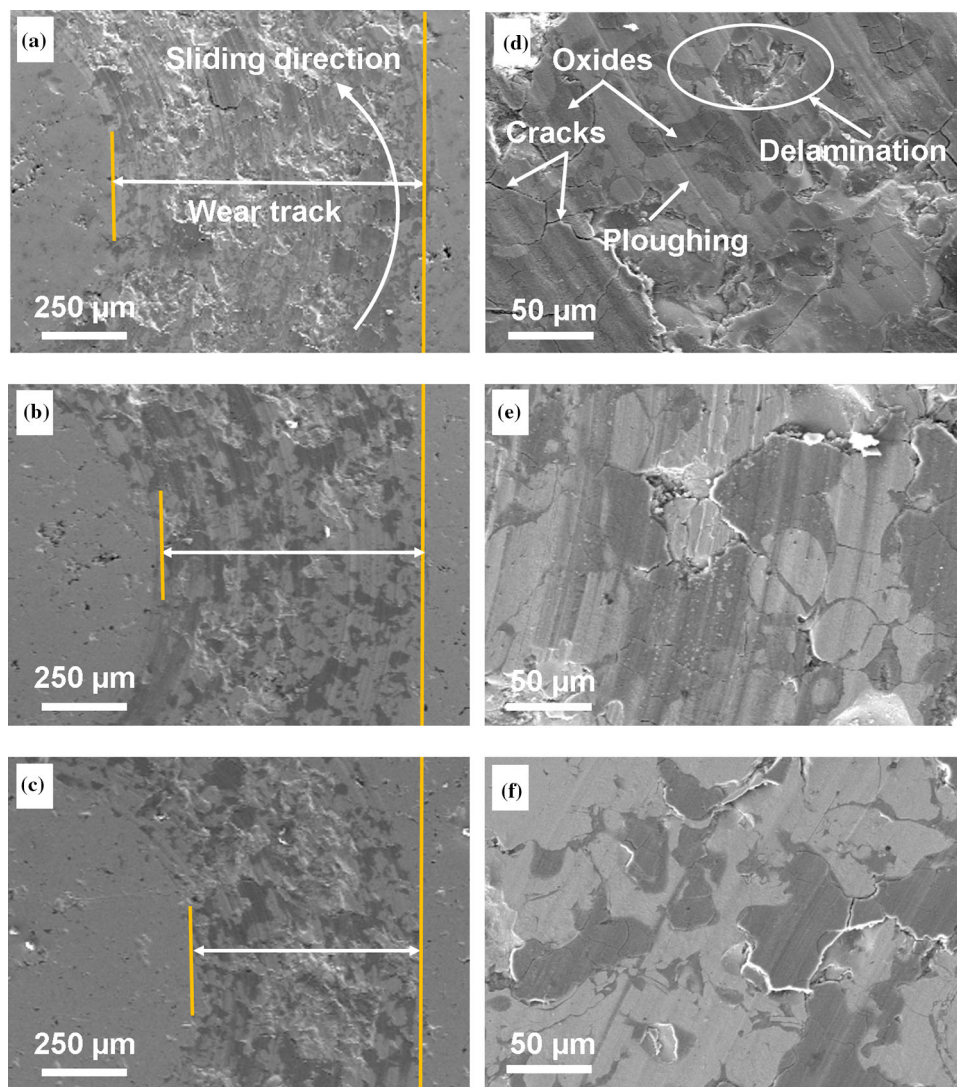


of a particular coating in rotating mode was less as compared to reciprocating mode, which was due to lower CoF, less debris particles on the wear track and low peak kinetic energy of the counter body in the rotating mode of wear test, which has been described above.

To understand the degradation mechanism during wear of the coatings, SEM study on the worn surfaces was carried out, and the results are shown in Fig. 9 and 10 corresponding to reciprocating and rotating modes of wear test, respectively. It can be observed from Fig. 9(a), (b) and (c) that the coating synthesized at lowest heat input (Coat-L) showed the widest wear track along with more delamination, cracks and oxide content, while coating synthesized at highest heat input (Coat-H) exhibited narrowest wear track. Wider wear track observed in Coat-L was due to poor inter-splat bonding and higher amount of porosity. Besides, the low proportion of intermetallic phases in Coat-L also resulted in inferior wear resistance compared to other coatings, as the presence of intermetallic phases in

the amorphous matrix hindered the shear band propagation and promoted generation of multiple shear bands, which eventually led to increase in the plasticity causing delayed cracking in the coating (Ref 24). Additionally, hard nanocrystalline intermetallic phases increase the hardness and scratch wear resistance (Ref 44, 46). Dry sliding wear can be correlated with scratch wear and therefore improvement in scratch wear resistance can enhance the macro-wear properties. It can be observed from the morphology of worn surfaces of the coatings shown in Fig. 9(d), (e) and (f) that they exhibit cracks and delamination. Porosity in the coatings acted as potential crack nucleating sites during sliding, which led to increase in the crack propagation, as wearing process proceeded leading to spallation of a layer of the coating called delamination. Such delamination in the coating indicates to wear caused by fatigue mode (Ref 47). Besides, the coating experienced continuous loading during sliding process, causing an increment in the local temperature of the tracks leading to

Fig. 10. Worn surface morphology of the coatings after rotating mode dry sliding wear test: (a, d) Coat-L, (b, e) Coat-M and (c, f) Coat-H



partial oxidation (Ref 31) at the surface. This is verified by elemental compositional analysis shown in Table 3 by EDS. It is to be noted that quantitative analysis by EDS is not very effective for elements with atomic mass less than 20 amu, as low atomic mass elements produce weak x-ray signals and therefore quantification of these elements by EDS is subjected to the resolution of the EDS detector. However, for qualitative and semiquantitative compositional analyses, EDS is proven to be a reliable spectroscopic technique for the detection of oxygen. These oxides tend to get delaminated during the process of further sliding. It should be pointed out here that there was a presence of slight abrasion on the worn surface of Coat-M and Coat-H, suggesting minor abrasion as a reason for wear loss. For the rotating mode of wear, it can be seen in Fig. 10 that the width of wear tracks followed the same trend as in reciprocating mode, but the wear damage and degree of oxidation were less severe compared to reciprocating sliding.

In reciprocating mode, peak sliding speed and frictional force were significantly high compared to rotating mode, which increased the flash temperature and led to higher extent of oxidation. However, the worn surface of the coatings in rotating mode exhibited primarily abrasive grooves, and the degree of abrasion decreased with increase in the heat input because of similar reasons mentioned in case of reciprocating wear. Moreover, the degree of delamination was so high during the reciprocating mode that abrasive wear became insignificant, in contrast to less delamination and severe abrasion for rotating mode. It is observed that overall wearing out process of the coatings under a particular mode is not only comprises of a single wear mechanism, rather a complex combination of different wear mechanisms with a dominant one amongst all the mechanisms. Additionally, it was noticed that the wear mechanisms did not change during a particular mode of wear for the different coatings, but the degree/extent of

Table 3. Composition of primary elements at the oxide-rich regions on the worn surfaces of the coatings under reciprocating and rotating mode of wear test

Element	Amount (wt.%)	
	Reciprocating mode	Rotating mode
Fe	8.4	10.4
Cr	10.6	13.2
Mo	9.6	12.3
O	59.9	45.3

those mechanisms varied considerably, while a transition in wear mechanism was observed upon changing the wear mode from reciprocating to rotating. This particular observation regarding the operation of multiple wear mechanisms has also been reported by several authors (Ref 35, 48, 49). Therefore, it can be concluded that the wear mechanism of all the coatings in reciprocating mode involves fatigue and oxidative wear accompanied by slight abrasive wear. On the contrary, the wear mechanism under rotating mode includes abrasive and oxidative wear along with fatigue wear.

Conclusions

Fe-based amorphous/nanocrystalline composite (Fe-ANC) coatings of composition Fe-10Cr-10Mo-4B-2C-4P (wt.%) were deposited on mild steel substrate by atmospheric plasma spraying (APS) under different spraying powers. This work focused on establishing a comprehensive understanding of difference in wear resistance along with the degradation mechanism during reciprocating and rotating modes of dry sliding wear of Fe-ANC coatings. The coatings majorly comprised of high amount of amorphous phase, ascribed to the high glass-forming ability of the chosen alloy system and high cooling rate in APS process. The salient conclusions of this work are as follows:

- Porosity and amorphous phase content of the coatings decreased with increasing heat input. Lower porosity content was ascribed to the higher degree of melting of feedstock powder on increasing heat input, which fill-up the inter-splats pores, while lower amorphous phase fraction was attributed to the higher heat input, leading to higher probability of crystallization at higher power.
- The enhanced hardness and wear resistance at higher heat input was attributed to the lower porosity content and higher amount of nano-sized hard intermetallic phases.

- Specific wear rate and coefficient of friction (CoF) obtained via rotating mode of sliding were found to be lower compared to those in rotating mode, attributed to lower amount of debris particles on the wear track and low peak kinetic energy of the counter body in the rotating mode of wear test.
- Most importantly, a transition in wear mechanism was envisaged under different modes of wear, viz. fatigue dominated in case of reciprocating mode to abrasion dominated for rotating mode.

Effect of various external loading conditions, like load, speed and distance on the transition in wear mechanism of during reciprocating and rotating mode of wear, particularly with respect to the subsurface deformation mechanisms should be investigated to strengthen understanding on wear behavior of such coatings.

Acknowledgments The author, T. Laha thankfully acknowledges Science and Engineering Research Board, Department of Science and Technology, Govt. of India (CRG/2020/000738) and Defence Research and Development Organisation, Govt. of India (ERIP/ER/202101002/M/01/1783) for financial support.

References

1. Q. Dong, J. Tan, R. Huang, H.L. Wang, P. Song, C.J. Li, Z.X. Feng, M. Calin and J. Eckert, Nanoindentation Creep Behavior of an Fe–Cr–Mo–B–C Amorphous Coating via Atmospheric Plasma Spraying, *Intermetallics*, 2022, **141**, p 107411. <https://doi.org/10.1016/j.intermet.2021.107411>
2. J.J. Kruzic, Bulk Metallic Glasses as Structural Materials: A Review, *Adv. Eng. Mater.*, 2016, **18**(8), p 1308–1331. <https://doi.org/10.1002/adem.201600066>
3. C. Suryanarayana and A. Inoue, *Bulk Metallic Glasses*, 2nd ed. CRC Press, Boca Raton, 2017. <https://doi.org/10.1201/9781315153483>
4. M. Miller and P. Liaw, *Bulk Metallic Glasses: An Overview*, 1st ed. Springer, New York, 2008. <https://doi.org/10.1007/978-0-387-48921-6>
5. N. Li, J. Zhang, W. Xing, D. Ouyang and L. Liu, 3D Printing of Fe-Based Bulk Metallic Glass Composites with Combined High Strength and Fracture Toughness, *Mater. Des.*, 2018, **143**, p 285–296. <https://doi.org/10.1016/j.matdes.2018.01.061>
6. S.K. Nayak, A. Kumar and T. Laha, Developing an Economical Wear and Corrosion Resistant Fe-Based Metallic Glass Composite Coating by Plasma and HVOF Spraying, *J. Therm. Spray Tech.*, 2022, **31**, p 1317–1329. <https://doi.org/10.1007/s11666-021-01277-w>
7. A. Inoue, F.L. Kong, S.L. Zhu, E. Shalaan and F.M. Al-Marzouki, Production Methods and Properties of Engineering Glassy Alloys and Composites, *Intermetallics*, 2015, **58**, p 20–30. <https://doi.org/10.1016/j.intermet.2014.11.001>
8. S.K. Nayak, A. Kumar and T. Laha, Fe-Based Metallic Glass Coatings by Thermal Spraying: A Focused Review on Corrosion Properties and Related Degradation Mechanisms, *Int. Mater. Rev.*, 2023, **68**(4), p 404–485. <https://doi.org/10.1080/09506608.2022.2084670>
9. W.J. Botta, J.E. Berger, C.S. Kiminami, V. Roche, R.P. Nogueira and C. Bolfarini, Corrosion Resistance of Fe-Based Amorphous

- Alloys, *J. Alloys Compd.*, 2014, **586**(1), p S105-S110. <https://doi.org/10.1016/j.jallcom.2012.12.130>
10. Z. Chu, W. Deng, X. Zheng, Y. Zhou, C. Zhang, J. Xu and L. Gao, Corrosion Mechanism of Plasma-Sprayed Fe-Based Amorphous Coatings with High Corrosion Resistance, *J. Therm. Spray Technol.*, 2020, **29**(5), p 1111-1118. <https://doi.org/10.1007/s11666-020-01030-9>
 11. P. Bijalwan, A. Kumar, S.K. Nayak, A. Banerjee, M. Dutta and T. Laha, Microstructure and Corrosion Behavior of Fe-Based Amorphous Composite Coatings Developed by Atmospheric Plasma Spraying, *J. Alloys Compd.*, 2019, **796**, p 47-54. <https://doi.org/10.1016/j.jallcom.2019.05.046>
 12. J. Zhou, X. Wang, J. You, J. Pang, X. Li and K. Qiu, Excellent Soft Magnetic Properties and Enhanced Glass Forming Ability of Fe-Si-B-C-Cu Nanocrystalline Alloys, *J. Alloys Compd.*, 2022, **918**, p 165538. <https://doi.org/10.1016/j.jallcom.2022.165538>
 13. D. Muraca, J. Silveyra, M. Pagnola and V. Cremaschi, Nanocrystals Magnetic Contribution to FINEMET-Type Soft Magnetic Materials with Ge Addition, *J. Magn. Magn. Mater.*, 2009, **321**(21), p 3640-3645. <https://doi.org/10.1016/j.jmmm.2009.07.005>
 14. F.C. Li, T. Liu, J.Y. Zhang, S. Shuang, Q. Wang, A.D. Wang, J.G. Wang and Y. Yang, Amorphous-Nanocrystalline Alloys: Fabrication, Properties, and Applications, *Mater. Today Adv.*, 2019, **4**, p 100027. <https://doi.org/10.1016/j.mtadv.2019.100027>
 15. L. Shi, X. Qin and K. Yao, Tailoring Soft Magnetic Properties of Fe-Based Amorphous Alloys through C Addition, *Prog. Nat. Sci. Mater. Int.*, 2020, **30**(2), p 208-212. <https://doi.org/10.1016/j.pnsc.2020.02.001>
 16. Z.B. Jiao, H.X. Li, J.E. Gao, Y. Wu and Z.P. Lu, Effects of Alloying Elements on Glass Formation, Mechanical and Soft-Magnetic Properties of Fe-Based Metallic Glasses, *Intermetallics*, 2011, **19**(10), p 1502-1508. <https://doi.org/10.1016/j.intermet.2011.05.020>
 17. S.K. Nayak, M.A. Faridi, G.M.A. Kumar and T. Laha, Fe-Based Metallic Glass Composite Coatings by HVOF Spraying: Influence of Mo on Phase Evolution, Wear and Corrosion Resistance, *Mater. Charact.*, 2022, **191**, p 112149. <https://doi.org/10.1016/j.matchar.2022.112149>
 18. S.L. Wang, H.X. Li, X.F. Zhang and S. Yi, Effects of Cr Contents in Fe-Based Bulk Metallic Glasses on the Glass Forming Ability and the Corrosion Resistance, *Mater. Chem. Phys.*, 2009, **113**(2–3), p 878-883. <https://doi.org/10.1016/j.matchemphys.2008.08.057>
 19. E. Coleman, Crystallization of Fe, Co and Ni Based Metallic Glasses, *Mater. Sci. Eng.*, 1976, **23**(2–3), p 161-167. [https://doi.org/10.1016/0025-5416\(76\)90187-7](https://doi.org/10.1016/0025-5416(76)90187-7)
 20. Ł. Szczepański, M. Bambach, F. Jensch, A. Ambroziak and T. Kurzynowski, Structural Investigations of Fe-Zr-Si-Cu Metallic Glass with Low Glass-Forming Ability Produced in Laser Powder Bed Fusion Technology, *Mater. Des.*, 2021, **210**, p 110112. <https://doi.org/10.1016/j.matdes.2021.110112>
 21. M. Naka, Effect of Metalloidal Elements on the Microhardness of Iron-Base Glasses, *J. Appl. Phys.*, 1980, **51**(11), p 6006-6009. <https://doi.org/10.1063/1.327522>
 22. M. Hasiak, M. Tkaczyk, A. Łaszcz and J. Olszewski, Effect of Alloying Additions on Microstructure, Mechanical and Magnetic Properties of Rapidly Cooled Bulk Fe-B-M-Cu (M = Ti, Mo and Mn) Alloys, *Metall. Mater. Trans. A*, 2022, **53**(2), p 556-572. <https://doi.org/10.1007/s11661-021-06530-z>
 23. C. Zhang, Q. Li, L. Xie, G. Zhang, B. Mu, C. Chang, H. Li and X. Ma, Development of Novel Fe-Based Bulk Metallic Glasses with Excellent Wear and Corrosion Resistance by Adjusting the Cr and Mo Contents, *Intermetallics*, 2023, **153**, p 107801. <https://doi.org/10.1016/j.intermet.2022.107801>
 24. B. Huang, C. Zhang, G. Zhang and H. Liao, Wear and Corrosion Resistant Performance of Thermal-Sprayed Fe-Based Amorphous Coatings: A Review, *Surf. Coat. Technol.*, 2019, **377**, p 124896. <https://doi.org/10.1016/j.surfcoat.2019.124896>
 25. S.F. Guo, L. Liu, N. Li and Y. Li, Fe-Based Bulk Metallic Glass Matrix Composite with Large Plasticity, *Scripta Mater.*, 2010, **62**(6), p 329-332. <https://doi.org/10.1016/j.scriptamat.2009.10.024>
 26. Z. Li, Z. Liu, Y. Wang, S. Liu, R. Jiang and Y. Wang, Fe-Based Amorphous Composite Coating Prepared by Plasma Remelting, *Adv. Mater. Sci. Eng.*, 2015, **2015**, p 375213. <https://doi.org/10.1155/2015/375213>
 27. M. Komaki, T. Mimura, Y. Kusumoto, R. Kurahasi, M. Kouzaki and T. Yamasaki, Formation of Fe-Based Amorphous Coating Films by Thermal Spraying Technique, *Mater. Trans.*, 2010, **51**(9), p 1581-1585. <https://doi.org/10.2320/matertrans.MAW201022>
 28. W. Guo, Y. Wu, J. Zhang, S. Hong, G. Li, G. Ying, J. Guo and Y. Qin, Fabrication and Characterization of Thermal-Sprayed Fe-Based Amorphous/Nanocrystalline Composite Coatings: An Overview, *J. Therm. Spray Technol.*, 2014, **23**(7), p 1157-1180. <https://doi.org/10.1007/s11666-014-0096-z>
 29. V. Varadaraajan, R.K. Guduru and P.S. Mohanty, Synthesis and Microstructural Evolution of Amorphous/Nanocrystalline Steel Coatings by Different Thermal-Spray Processes, *J. Therm. Spray Technol.*, 2013, **22**(4), p 452-462. <https://doi.org/10.1007/s11666-013-9885-z>
 30. F. Ghadami, A.S.R. Aghdam and S. Ghadami, Isothermal and Cyclic Oxidation Behavior of HVOF-Sprayed NiCoCrAlY Coatings: Comparative Investigations on the Conventional and Nanostructured Coatings, *J. Therm. Spray Technol.*, 2020, **29**, p 1926-1942. <https://doi.org/10.1007/s11666-020-01111-9>
 31. Z. Zhou, L. Wang, F.C. Wang, H.F. Zhang, Y.B. Liu and S.H. Xu, Formation and Corrosion Behavior of Fe-Based Amorphous Metallic Coatings by HVOF Thermal Spraying, *Surf. Coat. Technol.*, 2009, **204**(5), p 563-570. <https://doi.org/10.1016/j.surfcoat.2009.08.025>
 32. Y. An, G. Hou, J. Chen, X. Zhao, G. Liu, H. Zhou and J. Chen, Microstructure and Tribological Properties of Iron-Based Metallic Glass Coatings Prepared by Atmospheric Plasma Spraying, *Vacuum*, 2014, **107**, p 132-140. <https://doi.org/10.1016/j.vacuum.2014.04.021>
 33. F. Ghadami, M.A. Davoudabadi and S. Ghadami, Cyclic Oxidation Properties of the Nanocrystalline AlCrFeCoNi High-Entropy Alloy Coatings Applied by the Atmospheric Plasma Spraying Technique, *Coatings*, 2022, **12**(3), p 372. <https://doi.org/10.3390/coatings12030372>
 34. S. Vignesh, K. Shanmugam, V. Balasubramanian, K. Sridhar and D. Thirumalaikumarasamy, Electrochemical Corrosion Behaviour of HVOF Sprayed Iron-Based Amorphous Metallic Coatings on AISI 316 Stainless Steel in a NaCl Solution, *J. Mech. Behav. Mater.*, 2018, **27**(3–4), p 1-9. <https://doi.org/10.1515/jmbm-2018-0015>
 35. H. Guo, S. Zhang, W. Sun and J. Wang, Differences in Dry Sliding Wear Behavior between HVAF-Sprayed Amorphous Steel and Crystalline Stainless Steel Coatings, *J. Mater. Sci. Technol.*, 2019, **35**(5), p 865-874. <https://doi.org/10.1016/j.jmst.2018.11.006>
 36. J. Henao, A. Concustell, I.G. Cano, N. Cinca, S. Dosta and J.M. Guillemany, Influence of Cold Gas Spray Process Conditions on the Microstructure of Fe-Based Amorphous Coatings, *J. Alloys Compd.*, 2015, **622**, p 995-999. <https://doi.org/10.1016/j.jallcom.2014.11.037>
 37. H. Yuan, H. Zhai, W. Li, D. He, B. Cheng and L. Feng, Study of Dry Sliding Wear Behavior of a Fe-Based Amorphous Coating Synthesized by Detonation Spraying on an AZ31B Magnesium

- Alloy, *J. Mater. Eng. Perform.*, 2021, **30**(2), p 905-917. <https://doi.org/10.1007/s11665-020-05357-w>
38. J. Luo, N. Shi, Y.Z. Xing, C. Jiang and Y. Chen, Effect of Arc Power on the Wear and High-Temperature Oxidation Resistances of Plasma-Sprayed Fe-Based Amorphous Coatings, *High Temp. Mater. Process.*, 2019, **38**, p 639-646. <https://doi.org/10.1515/hmp-2019-0003>
39. A. Kumar, R. Kumar, P. Bijalwan, M. Dutta, A. Banerjee and T. Laha, Fe-Based Amorphous/Nanocrystalline Composite Coating by Plasma Spraying: Effect of Heat Input on Morphology, Phase Evolution and Mechanical Properties, *J. Alloys Compd.*, 2019, **771**, p 827-837. <https://doi.org/10.1016/j.jallcom.2018.09.024>
40. H.R. Ma, X.Y. Chen, J.W. Li, C.T. Chang, G. Wang, H. Li, X.M. Wang and R.W. Li, Fe-Based Amorphous Coating with High Corrosion and Wear Resistance, *Surf. Eng.*, 2017, **33**(1), p 56-62. <https://doi.org/10.1080/02670844.2016.1176718>
41. X. Li, H. Zhai, W. Li, S. Cui, W. Ning and X. Qiu, Dry Sliding Wear Behaviors of Fe-Based Amorphous Metallic Coating Synthesized by D-Gun Spray, *J. Non Cryst. Solids*, 2020, **537**, p 120018. <https://doi.org/10.1016/j.jnoncrysol.2020.120018>
42. R.S. Maurya, A.S. Sahu and T. Laha, Quantitative phase Analysis in $Al_{86}Ni_8Y_6$ Bulk Glassy Alloy Synthesized by Consolidating Mechanically Alloyed Amorphous Powder via Spark Plasma Sintering, *Mater. Des.*, 2016, **93**, p 96-103. <https://doi.org/10.1016/j.matdes.2015.12.129>
43. T. Gloriant, M. Gich, S. Suriñach, M.D. Baró and A.L. Greer, Evaluation of the Volume Fraction Crystallized during Devitrification of Al-Based Amorphous Alloys, *Mater. Sci. Forum*, 2000, **343**, p 365-370. <https://doi.org/10.4028/www.scientific.net/MSF.343-346.365>
44. A. Kumar, S.K. Nayak, P. Bijalwan, M. Dutta, A. Banerjee and T. Laha, Optimization of Mechanical and Corrosion Properties of Plasma Sprayed Low-Chromium Containing Fe-Based Amorphous/Nanocrystalline Composite Coating, *Surf. Coat. Technol.*, 2019, **370**, p 255-268. <https://doi.org/10.1016/j.surfcoat.2019.05.010>
45. S.K. Nayak, A. Kumar, A. Pathak, A. Banerjee and T. Laha, Multi-Scale Mechanical Properties of Fe-Based Amorphous/Nanocrystalline Composite Coating Synthesized by HVOF Spraying, *J. Alloys Compd.*, 2020, **825**, p 154120. <https://doi.org/10.1016/j.jallcom.2020.154120>
46. G.Y. Koga, T. Ferreira, Y. Guo, D.D. Coimbra, A.M. Jorge Jr., C.S. Kiminami, C. Bolfarini and W.J. Botta, Challenges in optimizing the resistance to corrosion and wear of amorphous Fe-Cr-Nb-B alloy containing crystalline phases, *J. Non-Cryst. Solids*, 2021, **555**, p 120537. <https://doi.org/10.1016/j.jnoncrysol.2020.120537>
47. A. Agarwal and N. Dahotre, Nanoindentation, Mechanical Properties of Laser-Deposited Composite Boride Coating Using Nanoindentation, *Metal. Mater. Trans. A*, 2000, **31**, p 401-408. <https://doi.org/10.1007/s11661-000-0277-x>
48. L. Xie, X. Xiong, Y. Zeng and Y. Wang, The Wear Properties and Mechanism of Detonation Sprayed Iron-Based Amorphous Coating, *Surf. Coatings Technol.*, 2019, **366**, p 146-155. <https://doi.org/10.1016/j.surfcoat.2019.03.028>
49. H. Zhang, Y. Xie, L. Huang, S. Huang, X. Zheng and G. Chen, Effect of Feedstock Particle Sizes on Wear Resistance of Plasma Sprayed Fe-Based Amorphous Coatings, *Surf. Coatings Technol.*, 2014, **258**, p 495-502. <https://doi.org/10.1016/j.surfcoat.2019.03.028>

Publisher's Note Springer Nature remains neutral with regard to jurisdictional claims in published maps and institutional affiliations.

Springer Nature or its licensor (e.g. a society or other partner) holds exclusive rights to this article under a publishing agreement with the author(s) or other rightsholder(s); author self-archiving of the accepted manuscript version of this article is solely governed by the terms of such publishing agreement and applicable law.